optica

Wireless THz link with optoelectronic transmitter and receiver: supplementary material

Tobias Harter[1,2], Sandeep Ummethala[1,2], Matthias Blaicher[1,2], Sascha Muehlbrandt[1,2], Stefan Wolf[1], Marco Weber[1], Md Mosaddek Hossain Adib[1], Juned. N. Kemal[1], Marco Merboldt[1], Florian Boes[3], Simon Nellen[4], Axel Tessmann[5], Martin Walther[5], Björn Globisch[4], Thomas Zwick[3], Wolfgang Freude[1], Sebastian Randel[1], Christian Koos[1,2*]

[1]*Institute of Photonics and Quantum Electronics (IPQ), Karlsruhe Institute of Technology (KIT), 76131 Karlsruhe, Germany*
[2]*Institute of Microstructure Technology (IMT), Karlsruhe Institute of Technology (KIT), 76344 Eggenstein-Leopoldshafen, Germany*
[3]*Institute of Radio Frequency Engineering and Electronics (IHE), Karlsruhe Institute of Technology (KIT), 76131 Karlsruhe, Germany*
[4]*Fraunhofer Institute for Telecommunications, Heinrich Hertz Institute (HHI), 10587 Berlin, Germany*
[5]*Fraunhofer Institute for Applied Solid State Physics (IAF), 79108 Freiburg, Germany*
**Corresponding author: christian.koos@kit.edu*

Published 13 August 2019

This document provides supplementary information to "Wireless THz link with optoelectronic transmitter and receiver," https://doi.org/10.1364/OPTICA.6.001063. It contains derivations of mathematical relations, details of the optoelectronic T-wave receiver implementation, as well as a discussion of the receiver conversion efficiency, bandwidth and noise. Furthermore, we give a comprehensive description of the wireless THz link including a characterization of the T-wave amplifiers and the uni-travelling-carrier photodiode (UTC-PD).

1. Mathematical model

In the main paper, we show coherent wireless THz communications using an optoelectronic receiver [1–3] and a tunable photonic local oscillator (LO). The concept of optoelectronic down-conversion in a photoconductive T-wave receiver (Rx) is illustrated in Fig. 2(a) of the main paper. In the following, we give a detailed derivation of the associated mathematical model.

The T-wave data signal from the transmitter (Tx) at an angular carrier frequency $\omega_S = 2\pi f_S$ is received by a bow-tie antenna resulting in a T-wave voltage across its feed points,

$$U(t) = \hat{U}_S(t)\cos\left(\omega_S t + \varphi_S(t)\right). \tag{S1}$$

In this relation, $\hat{U}_S(t)$ is the modulated T-wave voltage amplitude, and $\varphi_S(t)$ is the associated modulated phase. The antenna feed points are connected to a photoconductor G, which is illuminated by the superposition of two unmodulated optical fields $E_{LO,a}(t)$ and $E_{LO,b}(t)$ with frequencies $\omega_{LO,a}$, $\omega_{LO,b}$, amplitudes $\hat{E}_{LO,a}$, $\hat{E}_{LO,b}$, and phases $\varphi_{LO,a}$, $\varphi_{LO,b}$,

$$\begin{aligned} E_{LO,a}(t) &= \hat{E}_{LO,a}\cos\left(\omega_{LO,a}t + \varphi_{LO,a}\right), \\ E_{LO,b}(t) &= \hat{E}_{LO,b}\cos\left(\omega_{LO,b}t + \varphi_{LO,b}\right). \end{aligned} \tag{S2}$$

This leads to an optical power, which oscillates at a frequency $\omega_{LO} = \left|\omega_{LO,a} - \omega_{LO,b}\right|$ and has an amplitude $\hat{P}_{LO,1}$,

$$P_{LO}(t) = P_{LO,0} + \hat{P}_{LO,1}\cos\left(\omega_{LO}t + \varphi_{P,LO}\right). \tag{S3}$$

The quantities $P_{LO,0}$, $\hat{P}_{LO,1}$ are expressed by the (normalized) electrical field strengths, and the phase $\varphi_{P,LO}$ is given by the relative phases of the optical tones,

$$\begin{aligned} P_{LO,0} &= \tfrac{1}{2}\left(\hat{E}_{LO,a}^2 + \hat{E}_{LO,b}^2\right), \\ \hat{P}_{LO,1} &= \hat{E}_{LO,a}\hat{E}_{LO,b}, \\ \varphi_{P,LO} &= \varphi_{LO,a} - \varphi_{LO,b} \end{aligned} \tag{S4}$$

The photocarriers generated by the absorbed optical power change the photoconductance according to

$$G(t) = \mathcal{G}P_{LO}(t) = G_0 + \hat{G}_{LO}\cos\left(\omega_{LO}t + \varphi_{LO}\right), \tag{S5}$$

where $\mathcal{G}$ denotes a proportionality constant that describes the sensitivity of the photoconductor. Note that the phase φ_{LO} of the conductance oscillation might differ from the phase of the optical power oscillation $\varphi_{P,LO}$ in case the period of the LO power oscillation is of the same order of magnitude as the lifetime of the free carriers in

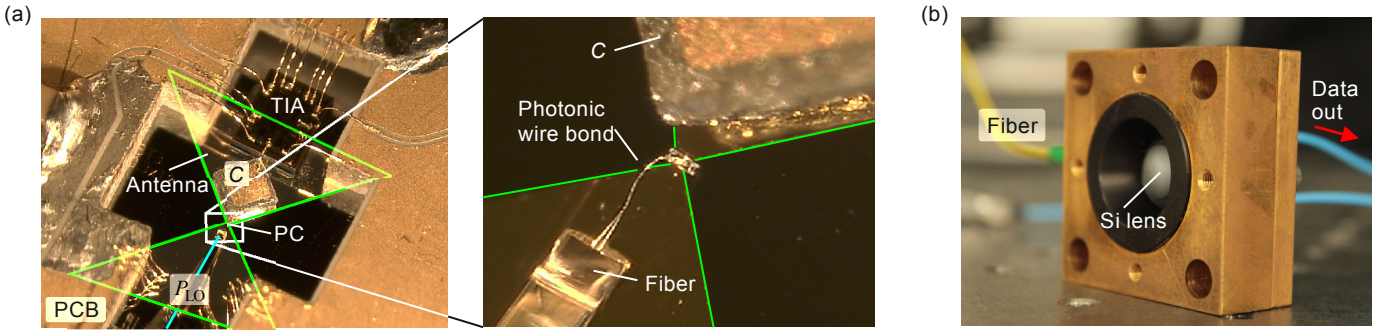

Fig. S1. Optoelectronic coherent T-wave Rx. **(a)** Microscope image of the Rx module. The photoconductor (PC) is connected to an on-chip bow-tie antenna, which is electrically bonded to a transimpedance amplifier (TIA). For better visibility, the contour of the bow-tie antenna is marked by green lines. The capacitor C = 1 nF is used to decoupled the photoconductor from the DC bias voltage that is supplied by the TIA at its input. Metal wire bonds are used to electrically connect the output of the TIA to a printed circuit board (PCB) consisting of a gold-plated alumina ceramic substrate. The PCB includes sub-miniature plugs for off-chip RF and DC connections. The photoconductor is illuminated by the time-dependent optical LO power $P_{LO}(t)$ through a fiber and a 3D-printed photonic wire bond, see inset for details. **(b)** Fully packaged Rx module. The photoconductor, antenna, TIA, and PCB are glued to a silicon lens for coupling the T-wave incident from below to the on-chip bow-tie antenna. All components are placed inside a metal housing for electromagnetic shielding of the Rx circuits. The photonic LO is fed to the Rx with a fiber. The down-converted data signal ("data out") is processed further by standard RF-equipment connected to the sub-miniature plugs on the PCB.

the photoconductor. The resulting current $I(t)$ through the photoconductor is then given by the product of the time-varying conductance $G(t)$ and the time-varying voltage $U(t)$,

$$\begin{aligned} I(t) &= G(t)U(t) \\ &= \underbrace{G_0\hat{U}_S(t)\cos\left(\omega_S t+\varphi_S(t)\right)}_{(1)} \\ &+ \underbrace{\tfrac{1}{2}\hat{G}_{LO}\hat{U}_S(t)\cos\left((\omega_S+\omega_{LO})t+\varphi_S(t)+\varphi_{LO}\right)}_{(2)} \\ &+ \underbrace{\tfrac{1}{2}\hat{G}_{LO}\hat{U}_S(t)\cos\left((\omega_S-\omega_{LO})t+\varphi_S(t)-\varphi_{LO}\right)}_{(3)}. \end{aligned} \quad \text{(S6)}$$

After amplification of the current $I(t)$ using a transimpedance amplifier (TIA), only the low-frequency-part (3) of Eq. (S6) remains. This leads to a down-converted current at the intermediate frequency $\omega_{IF}=|\omega_S-\omega_{LO}|$,

$$I_{IF}(t)=\tfrac{1}{2}\hat{G}_{LO}\hat{U}_S(t)\cos\left(\omega_{IF}t+\varphi_S(t)-\varphi_{LO}\right). \quad \text{(S7)}$$

The intermediate signal hence contains the amplitude and phase information of the T-wave data signal and can be processed by low-frequency electronics.

2. T-wave receiver

This section gives details of the implementation and the characterization of the optoelectronic Rx used in our experiments. Figure S1 shows images of our Rx module. The photoconductor [1,2] is connected to the feed points of the bow-tie antenna, see Fig. S1(a). The antenna is electrically bonded to a transimpedance amplifier (TIA, Maxim Integrated [4] PHY1097) for processing the down-converted intermediate-frequency current. Note that the TIA is originally designed for amplification of receiver signals in a passive optical network, where the photodiode is reverse-biased by the TIA. In our application, the photoconductor does not require a bias voltage and we hence use a capacitor C to decouple the photoconductor from the DC bias at the TIA input terminals. Metal wire bonds are used to electrically connect the output of the TIA to a printed circuit board (PCB) consisting of a gold-plated alumina ceramic substrate. The photoconductor is illuminated from the top with the time-dependent optical power $P_{LO}(t)$, which is coupled to the active region of the device from the horizontally positioned fiber by a photonic wire bond [5,6], see inset of Fig. S1(a). The assembly is placed on a silicon lens which focuses the T-wave incoming from below onto the antenna, see Fig. 2(c) of the main manuscript. All components are placed in a metal housing for electromagnetic shielding of the Rx circuits and for simplified handing of the assembly. The fully packaged Rx is shown in Fig. S1(b). The photonic LO is fed to the Rx with a fiber, and the down-converted RF data signal ("data out") is processed further by standard laboratory equipment. In the following, we give a detailed characterization of the Rx in terms of conversion efficiency, bandwidth, and noise.

Conversion efficiency

First we quantify the frequency-dependent response of the photoconductor connected to a bow-tie antenna. We define the conversion efficiency η as the ratio of the output power at the intermediate frequency in a $50\,\Omega$ load resistor related to the incident THz power P_{THz}. The conversion efficiency is measured with a photoconductor very similar to the one used for the data transmission experiment. Details are published elsewhere [1].

For this measurement, the same continuous-wave (c.w.) lasers are used for both the Tx and the Rx LO, i. e, $\omega_S=\omega_{LO}$. One of the Tx lasers is phase-modulated [7,8] by a saw-tooth signal with maximum amplitude of 2π and repetition period $2\pi/\omega_m$ where $\omega_m=2\pi\times 15\,\text{kHz}$. The resulting voltage at the Rx antenna feed points is then modulated according to Eq. (S1), $U(t)=\hat{U}_S\cos\left((\omega_S+\omega_m)t-\varphi_S\right)$. After down-conversion, the current according to Eq. (S7) becomes $I_{IF}(t)=\hat{I}_{IF}\cos\left(\omega_m t+\varphi_S-\varphi_{LO}\right)$ with $\hat{I}_{IF}=\tfrac{1}{2}\hat{G}_{LO}\hat{U}_S$. The current amplitude $\hat{I}_{IF}$ is measured with a lock-in amplifier (LIA) tuned to the modulation frequency ω_m. We change the T-wave frequency $\omega_S=\omega_{LO}$ and measure $\hat{I}_{IF}$ with the LIA along with the incident THz power P_{THz} using a calibrated pyroelectric thin film detector (Sensor- und Lasertechnik GmbH, THz20). The conversion efficiency η is then found as

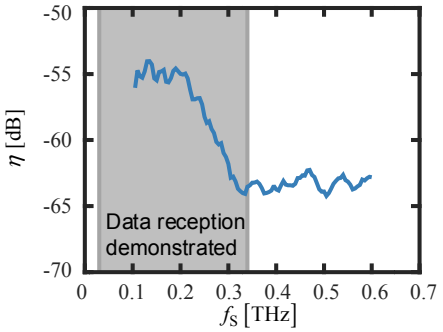

Fig. S2. Conversion efficiency of the photoconductive Rx for an optical power of $P_{\mathrm{LO},0} = \hat{P}_{\mathrm{LO},1} = 30\,\mathrm{mW}$. The gray area marks the frequency range that is used for the data transmission experiments. The conversion efficiency for frequencies larger than 0.34 THz is reduced by 10 dB, but remains constant up to at least 0.6 THz.

$$\eta = \frac{\frac{1}{2}\hat{I}_{\mathrm{IF}}^2 \times 50\,\Omega}{P_{\mathrm{THZ}}}. \qquad \text{(S8)}$$

In this relation, we model the photoconductor as an ideal current source driving a 50 Ω load impedance. This assumption is justified since the impedance of the photoconductor is much higher than the 50 Ω load, even under strong illumination. Figure S2 shows the conversion efficiency of the photoconductive Rx in dependence of the frequency f_S for an optical power of $P_{\mathrm{LO},0} = \hat{P}_{\mathrm{LO},1} = 30\,\mathrm{mW}$. The grey hatched area indicates the frequency range used in our experiments. In general, the T-wave bandwidth of a photoconductor is limited by the lifetime τ of the free carriers that are generated by the incident optical signal. This lifetime can be reduced by low-temperature growth of the associated III-V materials [2]. The frequency response of our device shows a roll-off of the conversion efficiency for frequencies beyond $f_{S,\tau} = 0.2\,\mathrm{THz}$, corresponding to a carrier lifetime of $\tau = 1/(2\pi f_{S,\tau}) = 0.8\,\mathrm{ps}$. The conversion efficiency drops by 10 dB and remains virtually constant for frequencies in the range $0.3\,\mathrm{THz} \le f_S \le 0.6\,\mathrm{THz}$.

We further investigate the dependence of the conversion efficiency $\eta(\hat{P}_{\mathrm{LO},1})$ on the LO power $\hat{P}_{\mathrm{LO},1} = P_{\mathrm{LO},0}$, see Fig. S3. At a T-wave frequency of 0.31 THz, we find a conversion efficiency η of – 63 dB at an LO power of $P_{\mathrm{LO},0} = \hat{P}_{\mathrm{LO},1} = 30\,\mathrm{mW}$. By measuring the LO-power-dependence of the root mean square (RMS) voltage $U_{\mathrm{S,RMS}}(\hat{P}_{\mathrm{LO},1})$ of the signal after the transimpedance amplifier, we can estimate the conversion efficiency for a certain LO power by

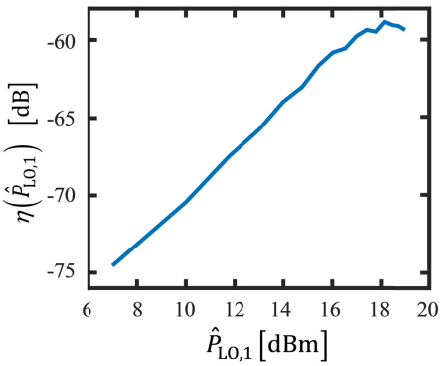

Fig. S3. Photoconductor conversion efficiency η as a function of the optical LO power $\hat{P}_{\mathrm{LO},1} = P_{\mathrm{LO},0}$ for a T-wave frequency of 0.31 THz.

$$\eta(\hat{P}_{\mathrm{LO},1}) = \eta(30\,\mathrm{mW}) \left(\frac{U_{\mathrm{S,RMS}}(\hat{P}_{\mathrm{LO},1})}{U_{\mathrm{S,RMS}}(30\,\mathrm{mW})} \right)^2. \qquad \text{(S9)}$$

In this relation, we use the fact that the oscillation amplitude $\hat{G}_{\mathrm{LO}}$ of the LO photoconductance and hence the current amplitude of $I_{\mathrm{IF}}(t)$ at the intermediate frequency increases in proportion to the optical LO power $\hat{P}_{\mathrm{LO},1} = P_{\mathrm{LO},0}$, see Eq. (S7). The current I_{IF} at the intermediate frequency is translated into a voltage signal at the output of the transimpedance amplifier, from which the RMS value is taken to obtain $U_{\mathrm{S,RMS}}(\hat{P}_{\mathrm{LO},1})$. For the devices used in our current experiments, the conversion efficiency can be increased by roughly 4 dB, if the LO power is increased from 30 mW to 60 mW. Note that the conversion efficiency of our current photoconductor saturates at high optical power levels – this aspect might be overcome in the future by optimized device design. The comparatively high optical LO power levels might be reduced to values of below 10 mW by using alternative device concepts such as plasmonic internal photoemission detectors [9].

Bandwidth

While the optoelectronic part of the T-wave Rx is extremely broadband, the maximum received data rate is limited by the TIA (Maxim Integrated, PHY1097 [4]) which is used for amplifying the down-converted signal $I_{\mathrm{IF}}(t)$. This device features a 3 dB bandwidth of 1.4 GHz, specified for a standard application scenario where the TIA is used in combination with a photodetector in a passive optical

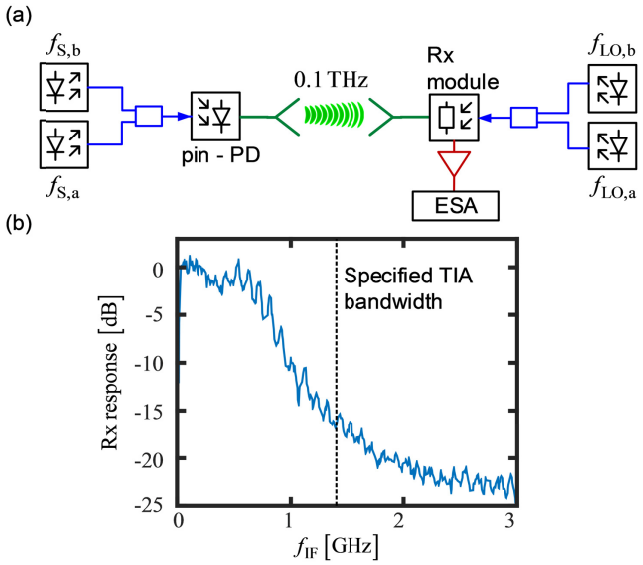

Fig. S4. IF frequency response of the Rx module. **(a)** Measurement setup. A continuous-wave (c.w.) T-wave tone at a constant frequency of $f_S = |f_{S,a} - f_{S,b}| = 0.1\,\mathrm{THz}$ is generated by photomixing of two optical c.w. laser tones. At the Rx, the T-wave signal is down-converted using a photonic local oscillator with frequency $f_{LO} = |f_{LO,a} - f_{LO,b}|$, which differs from f_S by the targeted intermediate frequency $f_{IF} = |f_S - f_{LO}|$. The power of the down-converted c.w. tone is measured by an electrical spectrum analyzer (ESA). By tuning the local oscillator frequency f_{LO}, we obtain the IF frequency response of the Rx. **(b)** Measured IF frequency response of the Rx module. The response drops quickly for frequencies beyond 0.75 GHz. The measured bandwidth is smaller than 1.4 GHz expected from the TIA specifications. We attribute this to fact that the impedance of the photoconductor connected to the TIA input differs from that of a high-speed photodiode, for which the device is optimized.

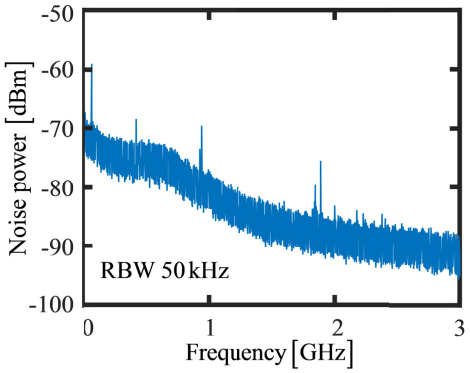

Fig. S5. Noise power measured at the output of the Rx without an incident T - wave. The optical LO power $P_{LO}(t)$ has an amplitude $P_{LO,0} = \hat{P}_{LO,1} = 80\,\text{mW}$ and oscillates a frequency $f_{LO} \approx 0.31\,\text{THz}$.

network. To measure the overall module bandwidth, we use the setup shown in Fig S4(a). A c.w. T-wave tone at a constant frequency $f_S = |f_{S,a} - f_{S,b}| = 0.1\,\text{THz}$ is generated. At the Rx, the T-wave tone is down-converted using a photonic local oscillator with frequency $f_{LO} = |f_{LO,a} - f_{LO,b}| \neq f_S$, Eq. (7). We then measure the power $\frac{1}{2}\hat{I}_{IF}^2 R_{TIA}$ of the down-converted IF tone at frequency $f_{IF} = |f_S - f_{LO}|$ using an electrical spectrum analyzer (ESA). By tuning the photonic LO frequency f_{LO}, the IF frequency response of the Rx module is obtained. The measured IF frequency response is normalized to its value in the frequency range between 100 MHz and 200 MHz, and the result is shown in Fig. S4(b). The Rx response is fairly constant up to 0.75 GHz and drops quickly for higher frequencies. The measured bandwidth is smaller than expected from the TIA specifications. We attribute this to fact that the impedance of the photoconductor connected to the TIA input differs from that of a high-speed photodiode, for which the device is optimized.

Noise

Figure S5 shows the noise characteristics of the packaged Rx module measured without an incident T-wave signal. The power was measured by an electrical spectrum analyzer connected to the Rx output. The photonic LO power $P_{LO}(t)$ has an amplitude $P_{LO,0} = \hat{P}_{LO,1} = 80\,\text{mW}$ and oscillates with frequency $f_{LO} \approx 0.31\,\text{THz}$. The noise power measured at the IF output of the Rx module drops significantly for increasing frequencies with a similar characteristic as the Rx response shown in Fig. S4 such that the signal-to-noise power ratio remains essentially constant. The origin of the strong frequency dependence of the Rx response and the Rx noise needs further investigation.

3. Wireless THz communication link

The detailed experimental setup used for the communication experiments is shown in Fig. S6(a). Tunable laser sources with line-width smaller than 100 kHz (Keysight, N7714A) are used to generate the optical tones for the Tx and the Rx. At the Tx, an arbitrary-waveform generator (AWG) is used to drive an IQ-modulator which is fed by an optical c.w. carrier with frequency $f_{S,a}$. As a data signal, we use a De-Bruijn sequence [10] of length 2^{13}. The optical signal is sent through an erbium-doped fiber amplifier (EDFA) followed by a 0.6 nm filter to suppress amplified spontaneous emission (ASE) noise. A 50/50-coupler combines the modulated carrier with an unmodulated c.w. tone at frequency $f_{S,b}$. To ensure strong interference of the two optical signals, we adjust the polarization using two polarization controllers (Pol. Contr.) by maximizing the power after a polarizer (Pol.). An optical attenuator (Att., Keysight N7764A) is used to set the power level $P_S(t)$, and a subsequent optical tap allows for measuring the optical spectra shown in Fig. 3(a) and Fig. 5(a) of the main manuscript. Finally, we adjust the polarization of the combined signal to maximize the current in a high-speed uni-travelling-carrier

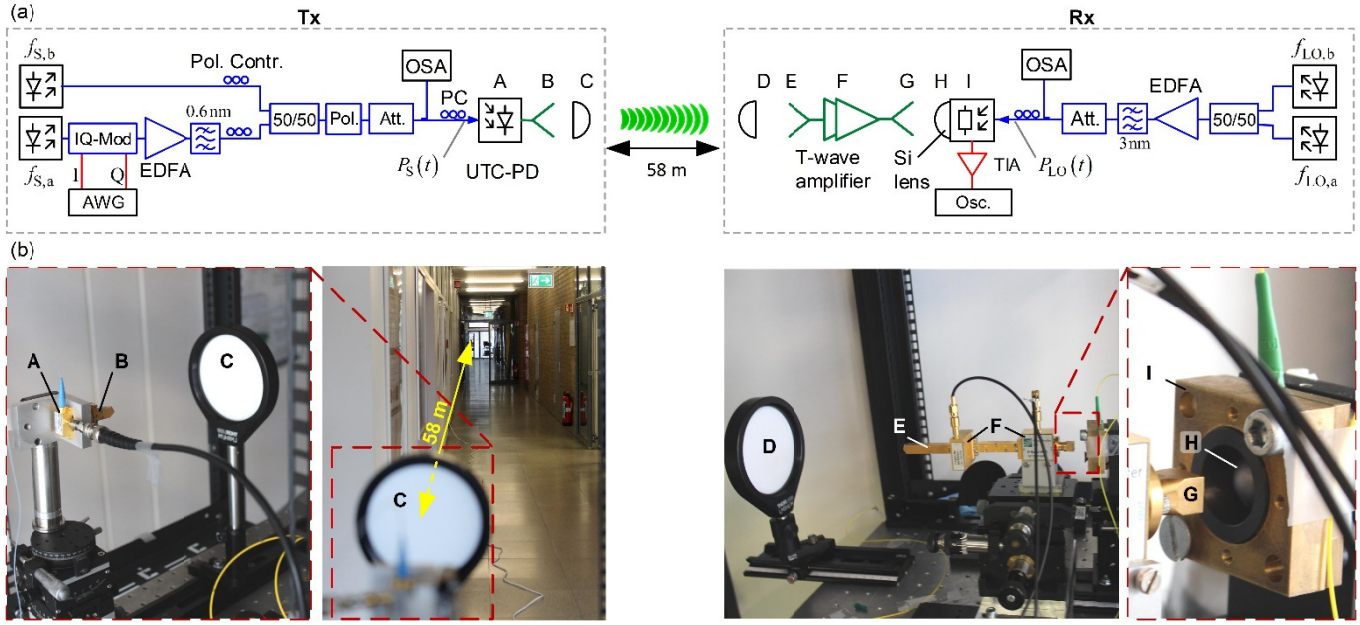

Fig. S6. Details of wireless data transmission link. **(a)** Schematic of the T-wave Tx and Rx used in our experiments. AWG: arbitrary-waveform generator; EDFA: Erbium-doped fiber amplifier; Pol.: Polarizer; Pol. Contr.: Polarization controller; Att.: Optical attenuator; OSA: Optical spectrum analyzer; PC: Polarization controller; TIA: Transimpedance amplifier; Osc.: Oscilloscope **(b)** Photograph of Tx and Rx. Components in the schematic of subfigure (a) are marked with letters A…I, which are used as labels in Subfigure (b). At the Tx, the UTC-PD (A), the horn antenna (B), and the PTFE lens (C) are shown. A distance of 58 m is bridged between the Tx and Rx. The Rx setup contains a second PTFE lens (D), a horn antenna (E), the cascaded T-wave amplifiers (F), as well as another horn antenna (G) and a subsequent silicon lens (H) for coupling the T-wave signal to the bow-tie antenna of the photoconductor (not shown) in the T-wave Rx module (I).

photodiode (UTC-PD). In the UTC-PD, the optical signal is converted to a T-wave signal with frequency $f_S = |f_{S,a} - f_{S,b}|$ (O/T - conversion). The T-wave is radiated to free space by a horn antenna and a subsequent Polytetrafluorethylen (PTFE) lens (Thorlabs, LAT200).

After a transmission distance of 58 m, the T-wave is captured by another PTFE lens and coupled to a WR 3.4 hollow waveguide by a horn antenna. The waveguide is connected to the input of two cascaded T–wave amplifiers [11,12], which compensate the free-space transmission loss and amplify the T-wave. In our current design, we use another horn antenna at the output of the second T-wave amplifier in combination with a silicon lens to couple the T-wave to the photoconductor. In the future, the performance of the scheme may be further improved by replacing this assembly with a waveguide-coupled photoconductor. For generating the photonic LO, two c.w. laser tones with optical frequencies $f_{LO,a}$ and $f_{LO,b}$ are superimposed using a polarization-maintaining 50/50 coupler, thus generating an optical power beat. The beat signal is amplified by an EDFA followed by a 3 nm filter to reduce ASE noise. A polarization controller is used to maximize the electric IF signal at the output of the polarization-sensitive photoconductor. The optical power P_{LO} coupled to the photoconductor can be adjusted by another optical attenuator (Att.), and a subsequent optical tap is used for measuring the optical spectra shown in Fig. 3(a) and Fig. 5(b) of the main manuscript. The down-converted IF signal is coupled to the TIA, the output voltage of which is sampled and stored in a real-time oscilloscope (Osc.) for further offline signal processing. Figure S6(b) shows a photograph of the wireless transmission link. The image on the left shows the Tx including the UTC-PD and the T-wave PTFE lens. The Rx is 58 m away from the Tx. On the right-hand image, the Rx including the T-wave PTFE lens, the T-wave amplifiers and the Rx module is shown in more detail. To facilitate identification of the components shown in the setup sketch of Fig. S6(a), we mark them with the letters A … I.

For finding optimum operation parameters, we characterize the performance of the wireless link shown in Fig. S6 for different optical powers $P_S(t)$ and powers $P_{LO}(t)$ at the Tx and the Rx,

$$P_S(t) = P_{S,0} + \hat{P}_{S,1}\cos\left(\omega_S t + \varphi_S(t)\right), \qquad f_S = |f_{S,a} - f_{S,b}|,$$
$$P_{LO}(t) = P_{LO,0} + \hat{P}_{LO,1}\cos\left(\omega_{LO} t + \varphi_{P,LO}\right), f_{LO} = |f_{LO,a} - f_{LO,b}|. \quad \text{(S10)}$$

In our measurements, we again adjust the c.w. lasers at the Tx and Rx such that the average power $P_{S,0}$ and $P_{LO,0}$ of the combined optical signal are equal to the amplitude $\hat{P}_{S,1}$ and $\hat{P}_{LO,1}$ of the respective power oscillation, $P_{S,0} = \hat{P}_{S,1}$ and $P_{LO,0} = \hat{P}_{LO,1}$. The Tx and Rx frequencies are set to $f_S = 0.310\,\text{THz}$ and $f_{LO} = 0.309\,\text{THz}$, respectively. For studying the transmission performance, we generate a quadrature phase-shift keying (QPSK) signal with a line rate of $R_b = 2\,\text{Gbit/s}$ at the Tx and measure its bit error ratio (BER) after down-conversion at the Rx.

Figure S7(a) shows the BER (red dots) obtained for various average powers $P_{S,0} = \hat{P}_{S,1}$ of the combined optical signal at the Tx and for a constant optical LO power of $P_{LO,0} = \hat{P}_{LO,1} = 80\,\text{mW}$ at the Rx. For some measurement points, the signal quality is that high that we could not measure any errors in a recording length of 10^5 symbols. We therefore estimate the BER from the error vector magnitude [13] (blue dots). For an optical power of $\hat{P}_{S,1} > 8\,\text{mW}$, the signal quality decreases because the T-wave amplifiers saturate, see constellation diagrams in the right-hand column of Fig. S7(a). In this case, we observe an asymmetric distribution of the noise around the various constellation points, see also Fig. 3(b) of the main manuscript, whereas a symmetric distribution is observed for low optical powers.

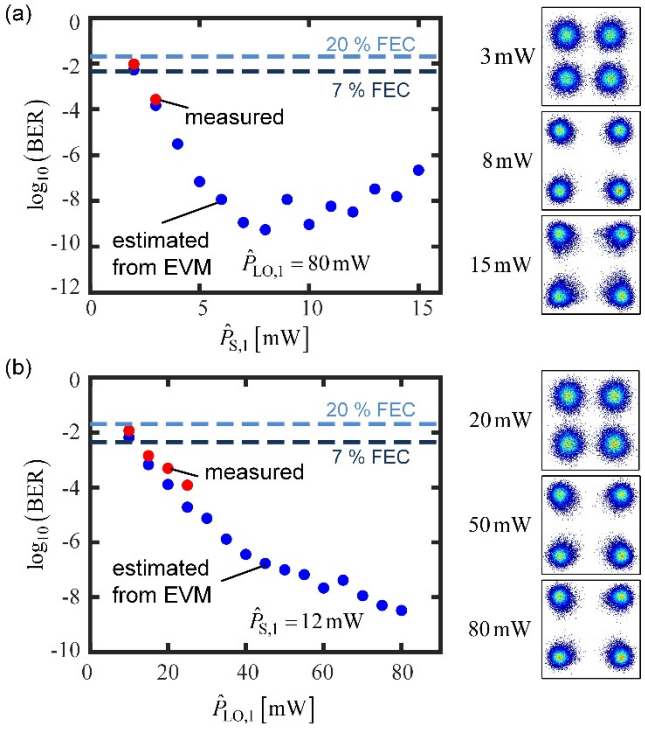

Fig. S7. Measured and estimated bit error ratio (BER) for different optical Tx and LO powers. As a test signal, we transmit a 1 GBd QPSK data signal. The T-wave carrier frequency is set to $f_S = 0.310\,\text{THz}$. **(a)** BER vs. optical power modulation amplitude $P_{S,0} = \hat{P}_{S,1}$ at the Tx. Red dots denote values that were directly measured, whereas blue dots refer to BER values estimated from the respective error vector magnitude (EVM). Since the length of our signal recordings was limited to 10^5 symbols, the lowest statistically reliable measured BER amounts to 10^{-4}. For measured BER values above this threshold, directly measured and estimated BER show good agreement, giving us confidence that the EVM-based estimations for BER < 10^{-4} are valid. **(b)** BER as a function of the LO power amplitude $P_{LO,0} = \hat{P}_{LO,1}$. The signal quality improves with increasing optical LO power $\hat{P}_{LO,1}$ and is finally limited by the maximum optical power that the photoconductor can withstand.

Figure S7(b) shows the BER measured for a 1 GBd QPSK signal at various average powers $P_{LO,0} = \hat{P}_{LO,1}$ of the combined optical LO signal at the Rx. In this case, the average power of the combined optical Tx signal is kept constant at $P_{S,0} = \hat{P}_{S,1} = 12\,\text{mW}$, close to its optimum point shown in Fig. S7(a). The signal quality improves with increasing optical LO power $\hat{P}_{LO,1}$ and is finally limited by the maximum optical power that the photoconductor can withstand. Figure S7 also indicates that higher-order modulation formats such as 16-state quadrature amplitude modulation (16QAM) might be within reach in future experiments: For a 1 GBd QPSK signal, we estimated a minimum BER of 10^{-9}, Fig. S7(a), corresponding to an SNR of roughly 16 dB when assuming that additive white Gaussian noise is the dominating impairment. From Fig. 10 of [14], this SNR would lead to a BER of roughly 3×10^{-3} for 16QAM, which would be below the threshold for FEC with 7 % coding overhead. With further improvements of the photoconductor and the transimpedance amplifiers, higher-order modulation formats might hence become possible.

If we distribute the T-wave power over multiple channels, see Section "Multi-channel transmission" of the main manuscript, the BER

degrades with increasing channel count. This is mostly caused by the fact that the overall signal power is limited by the T-wave amplifier cascade at the Rx and that hence the per-channel power decreases if more channels are used. This can be equivalently expressed by the degradation of the signal-to-noise power ratio (SNR) for the various channels. From the data shown in Fig. S5, we estimate a root-mean-square (RMS) voltage $\sigma_n = 19\,\text{mV}$ of the noise at the output of the transimpedance amplifier in a channel bandwidth of $B = 1\,\text{GHz}$ for the case without any T-wave signal. The corresponding SNR can then be estimated from the RMS voltage $U_{S,RMS}$ measured for each of the data channel when the T-wave signal is turned on,

$$\text{SNR} = \frac{U_{\text{S,RMS}}^2 - \sigma_n^2}{\sigma_n^2} \qquad \text{(S11)}$$

The SNR measured for the single-channel transmission at a data rate of $R_b = 1.5\,\text{Gbit/s}$ and for the multi-channel transmission with 6, 12 and 20 channels are shown in Fig. S8(a). With respect to the single-channel transmission, we expect an SNR reduction of 7.8 dB, 10.8 dB and 13 dB, respectively, through the splitting of the power among 6, 12, and 20 channels. This is in good agreement with our measurement, where we find an average SNR reduction of approximately 6.5 dB, 9.8 dB and 12.3 dB, respectively. For better comparison, we also show the corresponding BER measurements in Fig. S8(b), copied from Fig. 5(c) of the main manuscript. For the symbol rate of 0.75 GBd used here, the SNR degradation represents the main source of signal impairment, leading to a strong correlation of BER and SNR.

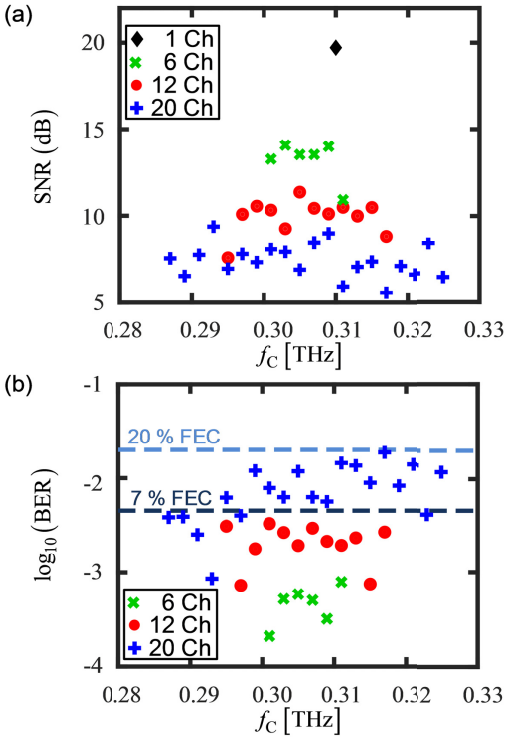

Fig. S8. Signal-to-noise power ratio (SNR) analysis for multi-channel transmission. **(a)** Measured SNR for 1, 6, 12 and 20 channels, each channel carrying a 0.75 GBd QPSK signal. Taking the single-channel transmission experiment as a reference, we find that the SNR reduces by approximately 6.5 dB, 9.8 dB, and 12.3 dB when splitting the limited T-wave power among 6, 12, and 20 channels, respectively. This is in good agreement with the theoretically expected values of 7.8 dB, 10.8 dB, and 13 dB. **(b)** For comparison, we also show the corresponding BER measurements, copied from Fig. 5(c) of the main manuscript. For the symbol rate of 0.75 GBd used here, the SNR degradation represents the main source of signal impairment, leading to a strong correlation of BER and SNR.

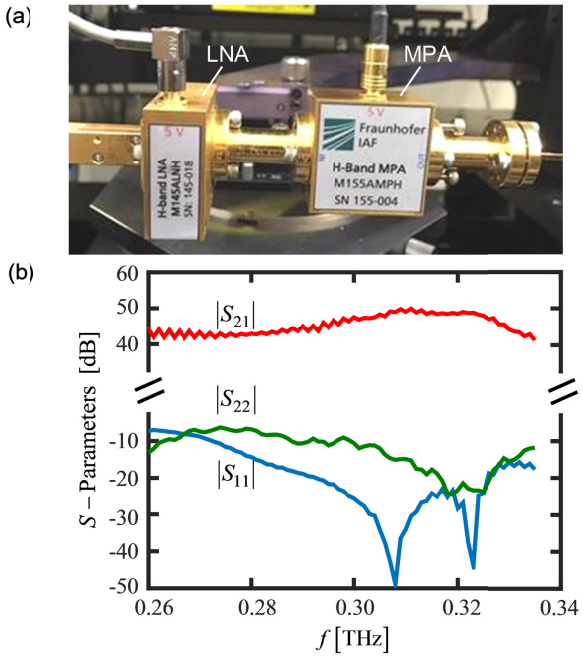

Fig. S9. Characterization of cascaded T-wave amplifiers. **(a)** Photograph of low-noise amplifier (LNA) and medium paper amplifier (MPA). **(b)** *S*-parameters measured by a vector network analyzer with frequency extension modules. A total gain of over 40 dB is achieved in a frequency range from 0.260 THz to 0.335 THz.

Fig. 5(c) of the main manuscript. For the symbol rate of 0.75 GBd used here, the bandwidth limitation of the TIA does not play an important role. Signal impairments are hence mainly dictated by the SNR degradation, and the BER is strongly correlated with the SNR.

4. T-wave amplifiers and UTC-PD

To compensate the free space T-wave transmission loss, we use a cascade of a low-noise amplifier (LNA) and a medium-power amplifier (MPA) [11,12], designed for operation in the submillimeter H-band (0.220 THz - 0.325 THz), see Fig. S9(a). The *S*-parameters for this cascade have been measured with a vector network analyzer (VNA) and are shown in Fig. S9(b). In a frequency range from 0.260 THz to 0.335 THz, the total gain is more than 40 dB.

To measure the frequency response of T-wave components and of the complete transmission system, we use the setups shown in Fig. S10. Two unmodulated c.w. laser tones having equal powers and different frequencies $f_{S,a}$ and $f_{S,b}$ are superimposed in a 50/50 combiner and coupled to the UTC-PD. The T-wave output power P_{THz} is measured in a calorimeter (VDI, Erickson PM4). By tuning the difference frequency $f_S = |f_{S,a} - f_{S,b}|$ of the two lasers, we measured the frequency-dependent output power of the UTC-PD without any amplifier, with the MPA, or with the cascade of LNA and MPA, Fig. S10(a,b,c). Furthermore, we measured the power after T-wave transmission over 58 m with the cascaded LNA and MPA at the Rx, Fig. S10(d). The results of all these measurements are shown in Fig. S10(e,f). Note that optical input power of the UTC-PD had to be strongly reduced for the case of the cascaded T – wave amplifiers without free-space link to prevent amplifier saturation. For evaluating the measurements, we use the fact that the T-wave output power of the UTC-PD is proportional to the square of the optical power,

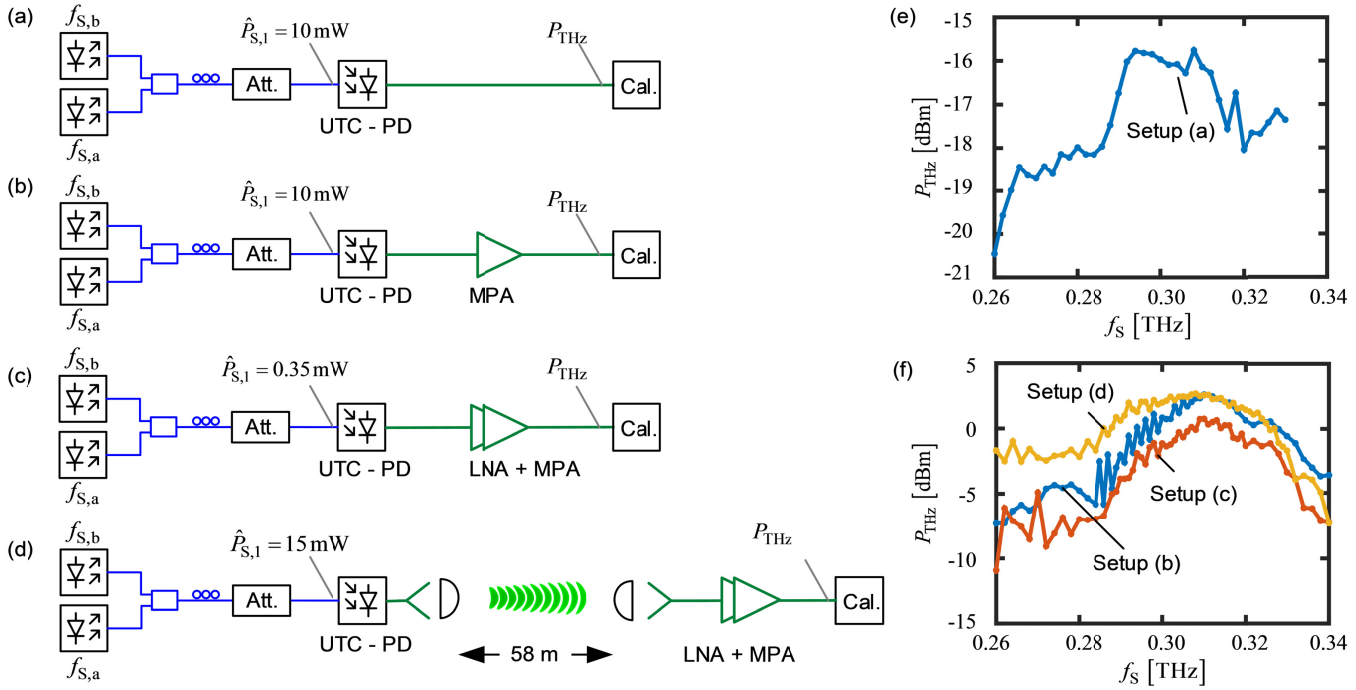

Fig. S10. Setup and results for measuring T-wave output power of UTC-PD and T-wave amplifiers. **(a)** Setup to measure T-wave output power P_{THz} of UTC-PD as a function of frequency $f_S = |f_{S,a} - f_{S,b}|$. **(b)** T-wave output power of UTC-PD and MPA. **(c)** T-wave output power of UTC-PD, LNA and MPA. **(d)** T-wave output power of UTC-PD, 58 m free space transmission, and LNA-MPA cascade. **(e)** Measured T-wave output power P_{THz} in dependence of Tx frequency f_S for UTC-PD. **(f)** Measured T-wave output power P_{THz} for UTC-PD and MPA, setup Fig. S10(b), for UTC-PD and LNA-MPA cascade, setup Fig. S10(c), and for UTC-PD, 58 m free space transmission and LNA-MPA cascade, setup Fig. S10(d).

$P_{THz} \propto \hat{P}_{s,1}^2$. This approach is valid because the UTC-PD is operated far from saturation. The received THz power after the amplifier cascade is more than 0 dBm in a frequency range from 0.29 THz to 0.33 THz for a transmission distance of 58 m. From the measurements shown in Fig. S10 we may also extract the gain of the T – wave amplifier cascade. This leads to a value of 45.5 dB, measured at a T – wave carrier frequency of 0.31 THz, which is in good agreement with the directly measured gain shown in Fig. S9.

According to the specifications in the datasheet, the LNA has a noise figure of $F_{LNA} = 10$ and a small-signal gain $G_{LNA} = 250$ (24 dB). The noise figure F_{MPA} of the MPA is not exactly known, but has the same order of magnitude as the LNA. According to the Friis formula,

$$F = F_{LNA} + \frac{F_{MPA} - 1}{G_{LNA}}, \qquad \text{(S12)}$$

the noise figure F of the cascaded LNA and MPA is dominated by the noise figure of the LNA and amounts to $F \approx 10$ (10 dB).

5. Link budget and noise analysis

In this section, we summarize the previous measurements and give a full link budget analysis. From the results shown in Fig. S10, we estimate the LNA gain, the MPA gain, and the total antenna gain of the two horn antennae and the two PTFE lenses that form the free-space transmission link. This analysis is performed at a T-wave frequency of f_S=0.31 THz. We measure an LNA gain of 27 dB and an MPA gain of 18.5 dB. The total antenna gain of the two horn/lens combinations is 87 dBi, which was estimated by comparing the received power with the calculated free-space path loss $FSPL_{dB}$ for a transmission distance of $d = 58$ m,

$$\mathrm{FSPL_{dB}} = 10\log\left(4\pi d\frac{f_S}{c}\right)^2 = 117\,\mathrm{dB}. \qquad \text{(S13)}$$

Note that the output of the T-wave amplifier cascade and the photoconductor are connected by a short free-space coupling section, see Fig. S6(a). This free-space section consists of a horn antenna at the MPA output and a Si lens for focusing the T-wave beam onto the on-chip bow-tie antenna connected to the photoconductor. While this configuration helped us to avoid laborious co-packaging of the components in our proof-of-concept experiment, it is not an ideal solution and introduces additional losses arising, e.g., from Fresnel reflections at the silicon lens surface, from an impedance mismatch between the bow-tie antenna and the photoconductor, and from the fact that the field generated by the horn antenna and focused to the bow-tie antenna by the silicon lens does not perfectly match the antenna mode. To quantify these losses and to thus estimate the expected performance improvement when using co-integrated devices, we have performed a 3D electromagnetic field simulation using a commercially available numerical time-domain solver (CST Microwave Studio, www.cst.com). see Fig. S11. To keep the numerical effort manageable, we have split the setup into two parts – the T-wave amplifier and the transmitting horn antenna on the one hand and the Si-lens, the receiving bow-tie antenna, and the photoconductor on the other hand. In a first step, we excite the horn antenna with a THz power of 2 mW, corresponding to the highest power of the amplifier cascade that could be measured at its output port using a waveguide-coupled calorimeter, and we record the electric field generated in a cross-sectional plane that is 15 mm away from the transmitting aperture of the horn antenna. In a second step, this field is then fed as an excitation into the simulation of the silicon lens, the bow-tie

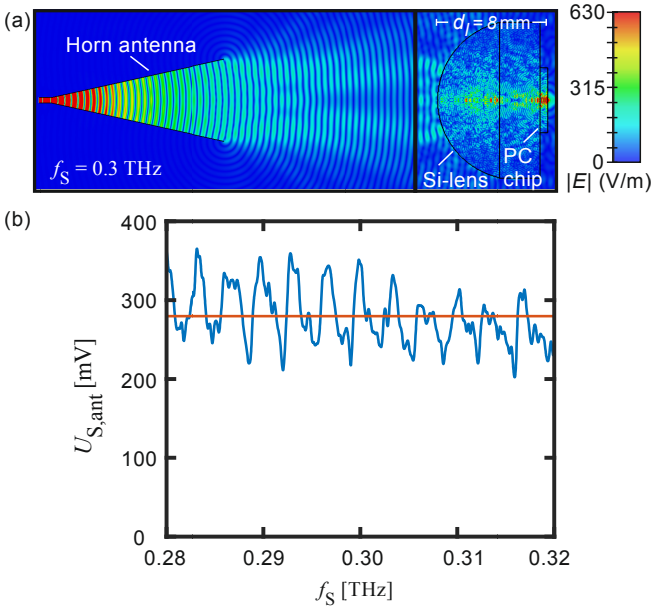

Fig. S11. Simulation of the free-space coupling section between the horn antenna and the photoconductor (PC). **(a)** Magnitude of the electric field at the cross-section of the transmission link for a T-wave power of 2 mW at the input of the horn antenna. To keep the numerical effort manageable, we split the simulation into two parts – the T-wave amplifier and the transmitting horn antenna on the left, and the Si-lens, the receiving bow-tie antenna, and the photoconductor on the right. **(b)** RMS value of the voltage effective across the photoconductor for a T-wave power of 2 mW at the input of the horn antenna. The pronounced ripples are attributed to standing waves within the Si lens. When averaging over the frequency range between 0.28 THz and 0.32 THz, we extract a mean RMS value of $U_{S,ant} = 281\,\text{mV}$ (red line) for the voltage across the photoconductor.

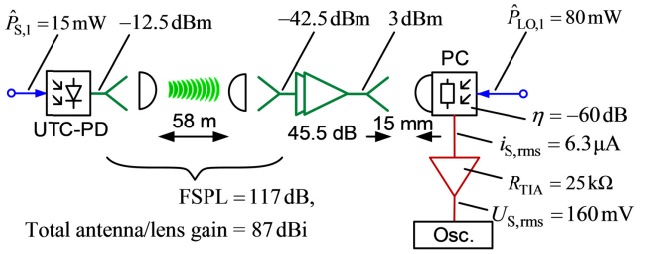

Fig. S12. Link budget for an optical power $\hat{P}_{S,1} = 15\,\text{mW}$ at the transmitter. Note that the conversion efficiency η of – 60 dB also contains the coupling losses introduced by the free-space section between the output of the T-wave amplifier cascade and the photoconductor.

antenna, and the photoconductor. In this simulation, we terminate the bow-tie antenna with a 750 Ω impedance, corresponding to the measured DC impedance of the photoconductor under an illumination with an optical LO power of $P_{LO,0} = 30\,\text{mW}$. The field distribution obtained from the two simulations for an T-wave power of 2 mW at the input of the horn antenna is shown in Fig. S11(a). From the simulation, we extract the frequency-dependent RMS value of the voltage that is effective across the photoconductor, see Fig. S11(b). We find pronounced variations of this voltage with respect to the T-wave frequency. These ripples exhibit a period of approximately 4 GHz and are attributed to standing waves that form in the Si lens, which features a thickness d_l of approximately 8 mm measured between the rear surface and the apex towards the horn antenna, see Fig. S11(a). Averaging the RMS voltage over a frequency range between 0.28 THz and 0.32 THz, we find a mean value of $U_{S,ant} = 281\,\text{mV}$, see the red horizontal line in Fig. S11(b). This value is then compared to the voltage amplitude of $U_{S,dir} = 1.22\,\text{V}$ that could be expected by coupling the 2 mW T-wave amplifier output to a 750 Ω termination. From the ratio of the two voltages, we extract a potential improvement of $10\log\left(U_{S,dir}^2 / U_{S,ant}^2\right) = 12.8\,\text{dB}$ that could be expected from a direct connection between the T-wave amplifier and the photoconductor with an appropriate impedance matching circuit. Direct coupling of the T-wave amplifier could avoid the interference ripples and hence also improve the uniformity of the frequency characteristic of the link. Note that the conversion efficiency shown in Fig. S2 was also measured with an antenna-coupled photoconductor on a silicon lens and therefore already includes the losses introduced by the free-space coupling section. Figure S12 shows a link budget for an optical power $\hat{P}_{S,1} = 15\,\text{mW}$ feeding the UTC-PD.

To estimate the influence of the T-wave amplifier noise, we calculate the thermal noise power P_n at the output of the cascaded T-wave amplifiers having a total noise figure of $F \approx 10$. For a signal bandwidth of $B = 1\,\text{GHz}$ and a power gain G corresponding to 45.5 dB, we find a T – wave noise power at the amplifier output of $P_n = 4kT_0FBG = 5.9\,\mu\text{W}$, corresponding to -22 dBm. Assuming a photoconductor conversion efficiency η from Eq. (S8) corresponding to –60 dB and a THz noise power $P_{THz} = P_n$, we can estimate the RMS of the noise current contribution $i_{n,RMS}$ in the baseband. To this end, we use the fact that the conversion efficiency was defined for a 50 Ω load impedance at the output of the photoconductor, which itself can be modeled as a current source due to its high internal impedance,

$$i_{n,RMS} = \sqrt{\frac{\eta P_n}{50\,\Omega}} = 340\,\text{nA}\,. \qquad \text{(S14)}$$

This noise contribution has the same order of magnitude as the typical input-referred noise of 150 nA specified in the data sheet of our TIA [4]. In the experiment, we actually measure a higher RMS noise current of 750 nA at the TIA input, see Fig. S5. We attribute the higher noise currents partially to the additional noise contribution of the photonic LO and partially to the fact that the photoconductor leads to a non-optimum impedance at the input of the TIA, which was designed for operation with-speed photodiodes. We expect that improvements of the photoconductor conversion efficiency, reduced coupling losses and better impedance matching between the T-wave amplifier and the photoconductor, as well as an improved design of the baseband circuitry connecting the photoconductor and the TIA will allow to greatly improve the signal-to-noise ratio of the scheme.

References

1. S. Nellen, B. Globisch, R. B. Kohlhaas, L. Liebermeister, and M. Schell, "Recent progress of continuous-wave terahertz systems for spectroscopy, non-destructive testing, and telecommunication," in *Proceedings of SPIE, 10531* (2018), p. 105310C.
2. T. Göbel, D. Stanze, B. Globisch, R. J. B. Dietz, H. Roehle, and M. Schell, "Telecom technology based continuous wave terahertz photomixing system with 105 decibel signal-to-noise ratio and 3.5 terahertz bandwidth," *Opt. Lett.* **38**, 4197–4199 (2013).
3. D. Stanze, A. Deninger, A. Roggenbuck, S. Schindler, M. Schlak, and B. Sartorius, "Compact cw terahertz spectrometer pumped at 1.5 µm wavelength," *J. Infrared Millim. Terahertz Waves* **32**, 225–232 (2011).

4. Maxim Integrated, "PHY1097," https://datasheets.maximintegrated.com/en/ds/PHY1097.pdf.
5. N. Lindenmann, S. Dottermusch, M. L. Goedecke, T. Hoose, M. R. Billah, T. P. Onanuga, A. Hofmann, W. Freude, and C. Koos, "Connecting Silicon Photonic Circuits to Multicore Fibers by Photonic Wire Bonding," *J. Lightwave Technol.* **33**, 755–760 (2015).
6. M. R. Billah, M. Blaicher, T. Hoose, P.-I. Dietrich, P. Marin-Palomo, N. Lindenmann, A. Nesic, A. Hofmann, U. Troppenz, M. Moehrle, S. Randel, W. Freude, and C. Koos, "Hybrid integration of silicon photonics circuits and InP lasers by photonic wire bonding," *Optica* **5**, 876–883 (2018).
7. D. Stanze, T. Göbel, R. J. B. Dietz, B. Sartorius, and M. Schell, "High-speed coherent CW terahertz spectrometer," *Electron. Lett.* **47**, 1292–1294 (2011).
8. T. Göbel, D. Schoenherr, C. Sydlo, M. Feiginov, P. Meissner, and H. L. Hartnagel, "Single-sampling-point coherent detection in continuous-wave photomixing terahertz systems," *Electron. Lett.* **45**, 65–66 (2009).
9. T. Harter, S. Muehlbrandt, S. Ummethala, A. Schmid, S. Nellen, L. Hahn, W. Freude, and C. Koos, "Silicon–plasmonic integrated circuits for terahertz signal generation and coherent detection," *Nat. Photonics* **12**, 625–633 (2018).
10. H. Badaoui, Y. Frignac, P. Ramantanis, B. E. Benkelfat, and M. Feham, "De Bruijn Pseudo Random Sequences Analysis For Modeling of Quaternary Modulation Formats," *J. Comput. Sci.* **7**, 35–38 (2010).
11. A. Tessmann, A. Leuther, V. Hurm, H. Massler, S. Wagner, M. Kuri, M. Zink, M. Riessle, H.-P. Stulz, M. Schlechtweg, and O. Ambacher, "A Broadband 220-320 GHz Medium Power Amplifier Module," in *2014 IEEE Compound Semiconductor Integrated Circuit Symposium (CSICS)* (IEEE, 2014), pp. 1–4.
12. A. Tessmann, A. Leuther, H. Massler, V. Hurm, M. Kuri, M. Zink, M. Riessle, and R. Loesch, "High-gain submillimeter-wave mHEMT amplifier MMICs," in *2010 IEEE MTT-S International Microwave Symposium* (IEEE, 2010), pp. 53–56.
13. R. Schmogrow, B. Nebendahl, M. Winter, A. Josten, D. Hillerkuss, S. Koenig, J. Meyer, M. Dreschmann, M. Huebner, C. Koos, J. Becker, W. Freude, and J. Leuthold, "Error Vector Magnitude as a Performance Measure for Advanced Modulation Formats," *IEEE Photonics Technol. Lett.* **24**, 61–63 (2012). Corrections: ibid. 24, 2198
14. R.-J. R.-J. Essiambre, G. Kramer, P. J. P. J. Winzer, G. J. G. J. Foschini, B. Goebel, P. J. P. J. Winzer, G. Kramer, and B. Goebel, "Capacity Limits of Optical Fiber Networks," *J. Lightwave Technol.* **28**, 662–701 (2010).